Applied Surface Science 545 (2021) 149032

Contents lists available at ScienceDirect

Applied Surface Science

journal homepage: www.elsevier.com/locate/apsusc

Full Length Article

A discovery of field-controlling selective adsorption for micro ZnO rods with unexpected piezoelectric catalytic performance

Fengping Peng [a,b], Haozhen Li [a], Wanxin Xu [a], Huihua Min [c], Zhenxuan Li [a], Feihu Li [a], Xiaogu Huang [a,b,*], Wei Wang [a,b,*], Chunhua Lu [b,*]

[a] Institute of Advanced Materials and Flexible Electronics (IAMFE), School of Chemistry and Materials Science, School of Environmental Science and Engineering, Nanjing University of Information Science & Technology, Nanjing 210044, PR China
[b] State Key Laboratory of Materials-Oriented Chemical Engineering, Jiangsu Collaborative Innovation Center for Advanced Inorganic Function Composites, Jiangsu National Synergetic Innovation Center for Advanced Materials (SICAM), Nanjing Tech University, Nanjing 210009, PR China
[c] Electronic Microscope Lab, Nanjing Forestry University, Nanjing 210009, PR China

ARTICLE INFO

Keywords:
Piezotronic effects
ZnO rods
Morphology
Selective adsorption
Catalysis

ABSTRACT

Exploring robust catalysts is the key to environmental protection. By the controllable exposure of polarization surfaces, the piezoelectric potential of ZnO was optimized, making micro ZnO rods, which have poor photocatalytic performance inherently, unexpectedly exhibit excellent piezoelectric catalytic performance. More importantly, an interesting phenomenon of field-controlling selective adsorption was discovered for the first time. This field-controlling selective adsorption made the ZnO rod work as a self-contained field controller, which can manipulate the migration of dye molecules according to the molecular polarity, enhancing the catalytic performance. Besides, this selective adsorption can help to relieve the hole-sensitive symptoms of ZnO, making ZnO more efficient and robust. Consequently, this study offers a new working prototype of selective adsorption for efficient catalysis.

1. Introduction

To explore robust catalytic technologies for water purification and environmental protection [1–4] has been an honorable mission endowed by the times. For half a century, photocatalysis, as a green catalytic technology, has triggered the research boom to protect the environment [5–7]. To date, despite the significant interest and considerable efforts paid, photocatalytic technology has an insurmountable shortcoming: it heavily relies on solar energy [8]. Yet, the light cannot be round-the-clock, and in many real situations, such as in the deep sea or other sewage systems, the light cannot go through, which enormously hampers the large-scale practical application. Consequently, game-changing research are required to overcome the current dilemma.

In 2010, Hong *et al.* unearthed an interesting phenomenon that through ultrasonic vibration of piezoelectric fibers, the stress-induced crystal polarization can drive the separation of free carriers to participate in catalytic reactions, achieving direct mechanical-to-chemical energy conversion [9]. The discovery makes catalysts evolve to such a state that catalytic reactions can be started by responding to mechanical waves from the environment, getting rid of the dependence on light. Since then, piezoelectric catalysis has been gradually coming into researchers' sight [10,11]. For instance, $BaTiO_3$ has been reported that it can degrade pigments and achieve tooth whitening [11]. Besides, some other piezoelectric materials (such as Bi_2WO_6 [12], $PbTiO_3$ [13]) have also been discovered to possess the capability of catalytic degradation in an aqueous sonication bath.

However, the current study is in infancy. There is little in-depth research to dig the piezoelectric-catalytic mechanism, which is important but poorly understood. At present, the understanding of the mechanism is generally at a shallow level: when the piezoelectric crystal is excited by mechanical stress, the positive and negative potential will be created on the opposite surface of the polarized crystal, being named as positive polarization domains (PPD) and negative polarization domains (NPD) respectively, and then the piezo-generated built-in electric field can be used to separate carriers for the catalytic degradation [14,15]. But there is no research to answer the deeper but neglected questions, such as how the morphology affects the piezoelectric-

* Corresponding authors at: Institute of Advanced Materials and Flexible Electronics (IAMFE), School of Chemistry and Materials Science, School of Environmental Science and Engineering, Nanjing University of Information Science & Technology, Nanjing 210044, PR China (X. Huang and W. Wang).
E-mail addresses: hxg@nuist.edu.cn (X. Huang), wwang@nuist.edu.cn (W. Wang), chhlu@njtech.edu.cn (C. Lu).

https://doi.org/10.1016/j.apsusc.2021.149032
Received 8 September 2020; Received in revised form 8 January 2021; Accepted 11 January 2021
Available online 13 January 2021

catalytic performance, how does the dye molecules behave under the piezoelectric field-controlling environment.

Herein, we choose ZnO, a typical piezoelectric material, to act as a piezoelectric catalyst model. By continuously tailoring the morphological structure, unearth the structure-performance relationship, which is greatly different from that in the photocatalysis. In addition, the typical cationic dyes, like Rhodamine B (RhB) and methylene blue (MB) [16], and anionic dye, like methyl orange (MO) [12], were chosen to detect the dye molecular behavior in the piezoelectric field. We for the first time find that the piezoelectric field can control the molecular behavior according to the molecular polarity: the dye molecules tend to be selectively adsorbed into the polarized surfaces with the opposite charge under the control of the piezoelectric field, achieving field-controlling selective adsorption, which can enhance the interaction between dye molecules and carriers, increasing the catalytic performance. In the system of ZnO and RhB, the hole-sensitive symptoms of ZnO can be relieved because this field-controlling selective adsorption can help to make full use of holes for catalysis. Furthermore, in the piezo/photocatalytic synergistic degradation process, the photo-corrosion can be relieved, and the piezo-generated built-in electric field can guide the migration of carriers and dye molecules, optimizing the catalytic performance. Therefore, our study provides a feasible and general strategy to construct various field-controlling systems for selective adsorption to enhance the desired performance.

2. Materials and methods

2.1. Materials

Zinc acetate dihydrate ($ZnAc_2$, ≥99.0%), hexamethylenetetramine (HMT, ≥99.0%), ethanol, methanol (CH_3OH, ≥99.7%), isopropyl alcohol (IPA, ≥99.7%), p-benzoquinone (BQ, ≥99.0%), Na_2SO_4(≥99.0%), acetic acid(≥99.7%), tetraethyl titanate ($Ti(OC_2H_5)_4$, ≥99.5%), NaOH(≥98%), $Ba(OH)_2{\cdot}8H_2O$(≥98%) were purchased from Sigma-Aldrich. Rhodamine B (RhB, ≥99.0%), methylene blue (MB, ≥98.5%), methyl orange (MO, ≥96%) were obtained from Tianjin Guangfu Fine Chemical Research Institute. All the chemicals were used as starting materials. Deionized water was used throughout the experiment.

2.2. Preparation

The preparation procedure for hexagonal ZnO crystals was as follows [17]. Zinc acetate dihydrate (3.0 g) and hexamethylenetetramine (1.92 g) were dissolved in 24 mL, 120 mL, 240 mL and 360 mL of deionized water, respectively. Keep these beakers covered by preservative films at 90 °C for 12 h. Wash the obtained white precipitates with deionized water and ethanol four times, respectively, and dry them at 60 °C for 12 h. At last, calcine the products at 200 °C for 2 h in the air. The prepared products were named as ZnO-24, ZnO-120, ZnO-240 and ZnO-360, respectively.

The preparation of $BaTiO_3$ was as follows. Typically, 25 mL Ti $(OC_2H_5)_4$ was dropped into 1.0 M acetic acid solution to prepare titanium precursor $Ti(OH)_4$. After 72 h, wash the precipitate with water and then dry at 60 °C. Then add the prepared $Ti(OH)_4$ and $Ba(OH)_2{\cdot}8H_2O$ (molar ratio Ti: Ba = 1:1) into 0.25 M NaOH solution. After being stirred for 30 min, the above solutions (60 mL) were transferred into the polytetrafluoroethylene reactors and then put reactors at 200 °C for 6 h. When cooled to room temperature, the white precipitates were washed with water for three times.

2.3. Characterization

The morphological observation was measured on a field emission scanning electron microscope (FESEM, JSM-7600F) and a transmission electron microscopy (TEM). The XRD patterns were recorded on a Lab XRD-6100 X-ray diffractometer (Shimadzu) with Cu Kα radiation (λ = 0.1541 nm). Piezoelectric force microscopy (PFM) measurements were performed using Bruker Dimension ICON. Photoluminescence (PL) spectroscopy was performed on a fluorescence spectrophotometer (Cary Eclipse, Agilent) using 325 nm emission.

2.4. Catalytic degradation of organic dyes, such as RhB, MB, and MO

To evaluate the catalytic activities of samples, a series of experiments were carried out. Typically, each sample (0.2 g) was dispersed into 200 mL of 10 mg/L dye solution in a quartz reactor, which was surrounded by cooling water.

For photocatalysis, the quartz reactor was illuminated by a 300 W xenon lamp.

As for the piezoelectric catalysis, the quartz reactor was put in an ultrasonic cleaner (40 kHz, power-adjustable, max: 300 W) equipped with an electric stirrer. For the sake of shielding against the light, the ultrasonic cleaner was covered by the photomask.

During the measurement, the suspension was kept in the dark for 30 min. Then the catalytic reaction was initiated with ultrasonic and light waves for piezoelectric-catalysis and photocatalysis, respectively. 4 mL of the suspension was taken at given time intervals during the catalytic process. All the suspension samples were separated through centrifugation, and then the absorbance of the solution was recorded using a Cary 5000 UV–vis spectrophotometer by monitoring the absorption spectrum of each dye. The degradation efficiency was reported as C/C_0 (C and C_0 are the peak intensity of the adsorption spectra measured at different time t and the beginning, respectively).

2.5. Detection of active species

Active species trapping experiments were conducted as follows. 1.0 mM CH_3OH, IPA, BQ, and Na_2SO_4 were chosen as the quenchers of the hole (h^+) [18], hydroxyl radical ($^{\cdot}OH$) [19], superoxide radical ($^{\cdot}O_2^-$) [19], the electron (e^-) [20–24] respectively. The procedures were just the same as the above process of degradation except for the addition of quenchers.

2.6. Piezoelectrochemical assessment

The piezoelectrochemical assessment of the samples was performed by an electrochemical workstation (CHI600E, Shanghai) using Ag/AgCl and Pt as the reference electrode and the counter electrode, respectively. The prepared samples acted as the working electrodes. The current of the working electrodes was recorded with or without sonication conditions (300 W, 40 kHz) for 10 s, respectively.

3. Results and discussion

3.1. Morphology, structure and piezoeletric properties

The rod-like structure is the most common morphology among the various ZnO crystals [25,26]. It is well known that ZnO rods along the *c*-axis direction can contribute to the exposure of side surfaces, which are more sensitive to force, serving as polarization surfaces [27]. When subjected to force, ZnO rods will be polarized, creating positive and negative potentials at the opposite side surfaces [28]. Thus, to expose polarization surfaces, the morphologies were tailored by directing the growth of ZnO crystals. As Fig. 1a-d show, the highest precursor concentration can help the formation of oblate-like particles with a diameter of about 70 nm. When the precursor concentration declines, the ZnO shapes change from particles into hexagonal prismatic rods with the lengths of about 4.13, 4.48, 8.79 μm and the diameters of about 3.18, 1.95, 2.54 μm for ZnO-120, ZnO-240, and ZnO-360, respectively (Table S1). Accordingly, the length-to-diameter aspect ratio (Table S1) increases monotonically from ZnO-120 to ZnO-360, causing more side

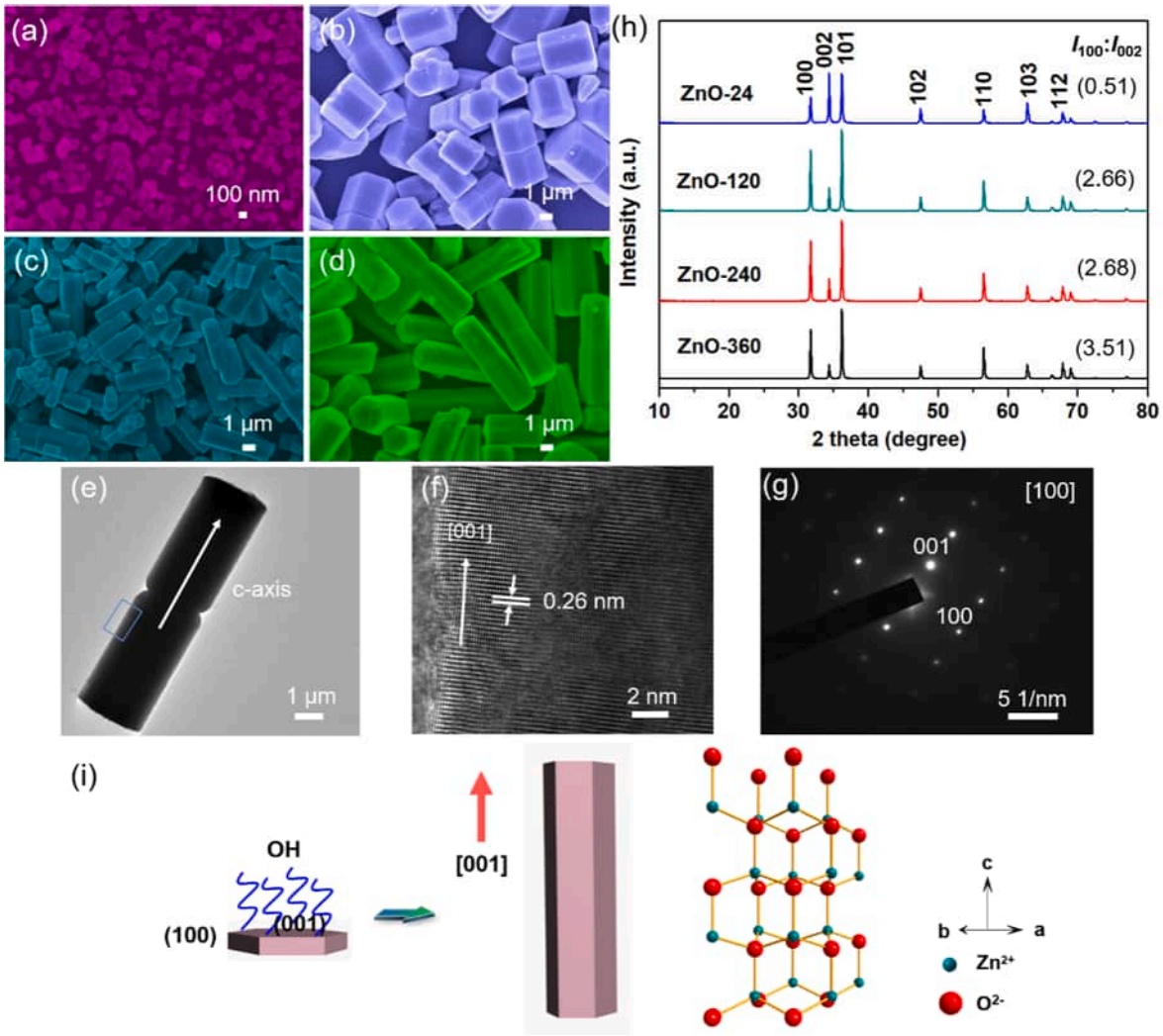

Fig. 1. FESEM images of (a) ZnO-24, (b) ZnO-120, (c) ZnO-240, and (d) ZnO-360; (e) TEM image, (f) HRTEM image and (g) the corresponding SAED pattern of ZnO-360; (h) XRD patterns of the ZnO-24, ZnO-120, ZnO-240 and ZnO-360 catalysts; (i) schematic illustration of the growth models of the ZnO rod.

surfaces to be exposed.

Then TEM was performed to elucidate the atomic structure of ZnO-360 crystal. Fig. 1e is the side view of the prepared ZnO-360 rod. Perpendicular to the rod, the lattice spacing (Fig. 1f) is ca. 0.26 nm, which can be ascribed to the (0 0 1) polar plane [26,29], indicating the growth direction along *c*-axis [30]. The corresponding selected area electron diffraction (SAED) pattern (Fig. 1g) can be indexed as the [1 0 0] zone spots of hexagonal ZnO [31] and reflects the single-crystalline nature of the ZnO rods. In general, the prepared ZnO rods are elongated in the [0 0 1] direction, and leave behind (1 0 0) facets exposed on the side surfaces.

Besides, XRD patterns were also recorded to further monitor the crystallographic structure. As Fig. 1h shows, the diffraction peaks of all samples match well with the hexagonal piezoelectric structure of ZnO (JCPDS 36-1451). Also, the peaks are very sharp, which evidences the high crystal quality of ZnO. Furthermore, with the decreasing precursor concentration, the calculated values of I_{100}: I_{002} increase monotonically from 0.51 to 3.51, suggesting that the proportion of (1 0 0) facets exposed on the side surface increases due to the preferential growth in the [0 0 1] direction. This means the larger proportion of polarization surfaces have been formed in polarized ZnO rods, which is consistent with FESEM and TEM observation.

The above results indicate that the precursor concentration makes a remarkable influence on the morphologies of ZnO (Fig. 1i). During the hydrothermal process, zinc acetate and HMT provide CH_3COO^- and OH^- ions, respectively [17,32]. At higher precursor concentration, more CH_3COO^- ions tend to adsorb on the Zn^{2+}-terminated (0 0 1) polar plane [33], suppressing crystal growth in the [0 0 1] direction. Thus, the shape of ZnO-24 is oblate-like. When the precursor concentration declines, OH^- ions will substitute CH_3COO^- ions to adsorb on the (0 0 1) plane as the precipitant [34], facilitating preferential growth along the *c*-axis, leaving behind the (1 0 0) facets as the main crystal planes of ZnO rods (Fig. 1). Thence, if the ZnO rod extends in the [0 0 1] direction, the fraction of (1 0 0) facets will increase, denoting a larger proportion of polarization surfaces in polarized ZnO rods.

The PFM was performed to confirm the piezoelectric property of ZnO rods. This technique (Fig. 2a) is based on the detection of local shape deformation in response to an external electrical voltage due to the electro-strictive effect [35]. Fig. 2b shows the typical three-dimensional morphology of ZnO rods. The amplitude and phase maps are shown in Fig. 2c and e. The hysteretic amplitude versus bias voltage exhibits a standard ferroelectric butterfly loop, and signifies the apparent variation in the amplitude (Fig. 2d) owing to the changing strain with an applied ramp voltage. This certifies the piezoelectric property of the ZnO rods. Besides, the phase curve (Fig. 2f) is well-matched with the amplitude curve and displays an approximately 180° switching. The switching behavior is the direct embodiment of the piezoelectric characteristic, which is in accordance with the piezoelectric crystal structure proved by

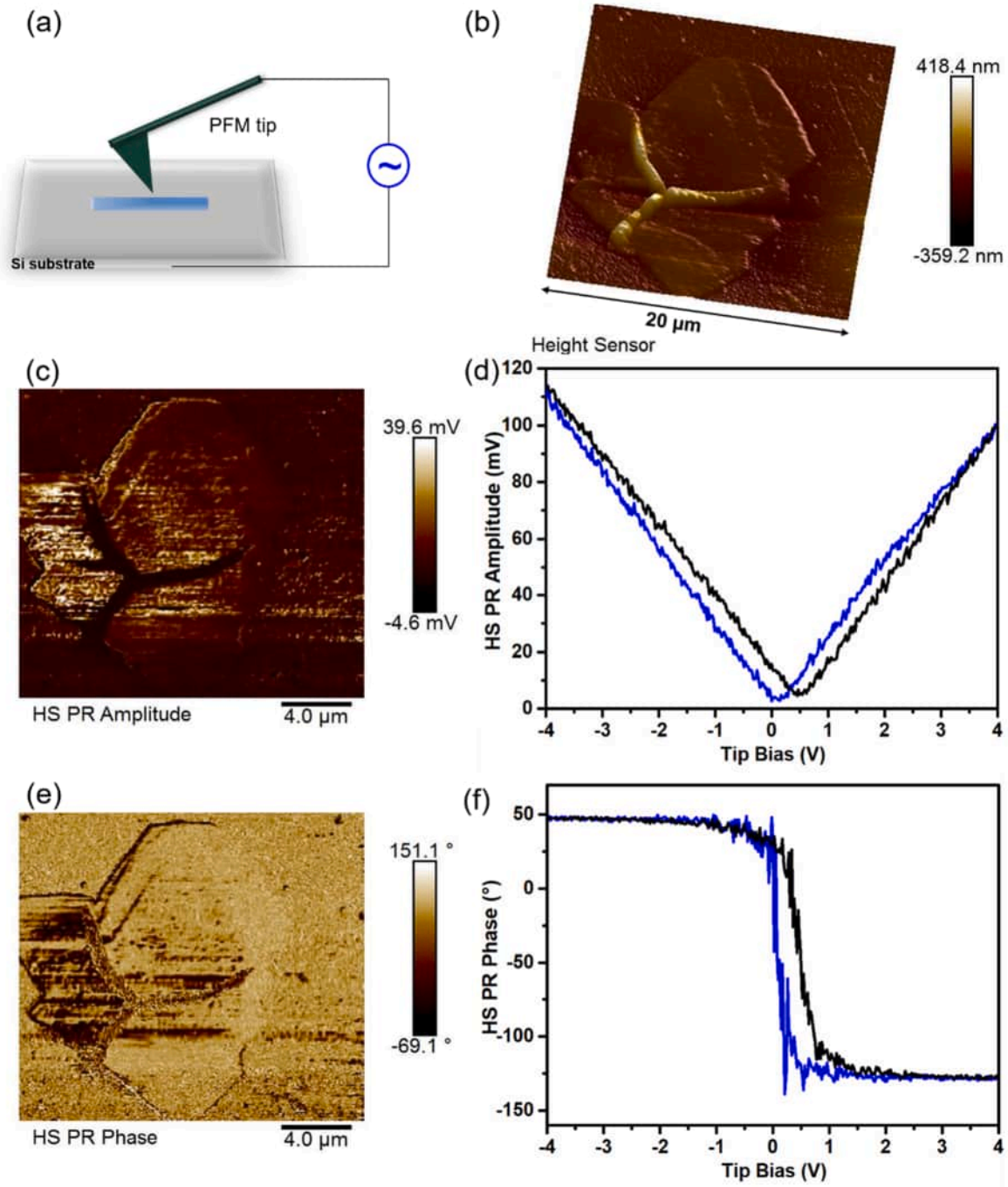

Fig. 2. (a) Schematic of the PFM setup for the ZnO-360 rods; (b) PFM morphology, (c) the relative amplitude of the piezoelectric response, (e) the phase of the piezoelectric response; (d) the standard piezoelectric amplitude curve and (f) the phase curve.

XRD.

To further study the relationship between morphologies and piezoelectric properties, the finite element method (FEM) was used to calculate the piezoelectric potential distribution and output. In Fig. 3a, the length and diameter are $l = 8.79$ μm and d = 2.54 μm, respectively. According to sonication conditions (300 W, 40 kHz), the applied stress is chosen as 60 KPa. The material constants used in the calculation are elastic constants c11 = 209.7 GPa, c12 = 121.1 GPa, c13 = 105.4 GPa, c23 = 105.4 GPa, c33 = 211 GPa, c44 = 42.4 GPa, and c55 = 42.4 GPa, piezoelectric constants e15 = −0.48 C/m^2, e31 = −0.57 C/m^2, and e33 = 1.32 C/m^2. The relative dielectric constants are $\kappa^r_\perp = 8.54$ and $\kappa^r_\parallel = 10.2$. Fig. 3a shows the potential distribution of ZnO-360 at its side cross-section parallel to its *c*-axis. By finite element analysis, it is apparent that when the ZnO rod is subjected to the ultrasonic wave, the positive and negative potential will be created at the opposite side surfaces, generating a potential drop. In addition, the potential values increase from ZnO-24 to ZnO-360 (Fig. 3b). This is because the larger the proportion of polarization surfaces is, the greater the piezoelectric potential can be generated [27,36], the higher piezoelectric current can be formed (the inset image of Fig. 3b).

An atomic mode (Fig. 3c-d) is used to elaborate on the inversion of stress into electricity [37]. Typical wurtzite ZnO crystal structure belongs to the space group $P6_3mc$, and each Zn^{2+} cation is surrounded by four O^{2-} anions with two lattice parameters *a* (3.2489 Å) and *c* (5.2049 Å), as shown in Fig. 3c. Thus, wurtzite ZnO holds an asymmetric crystal

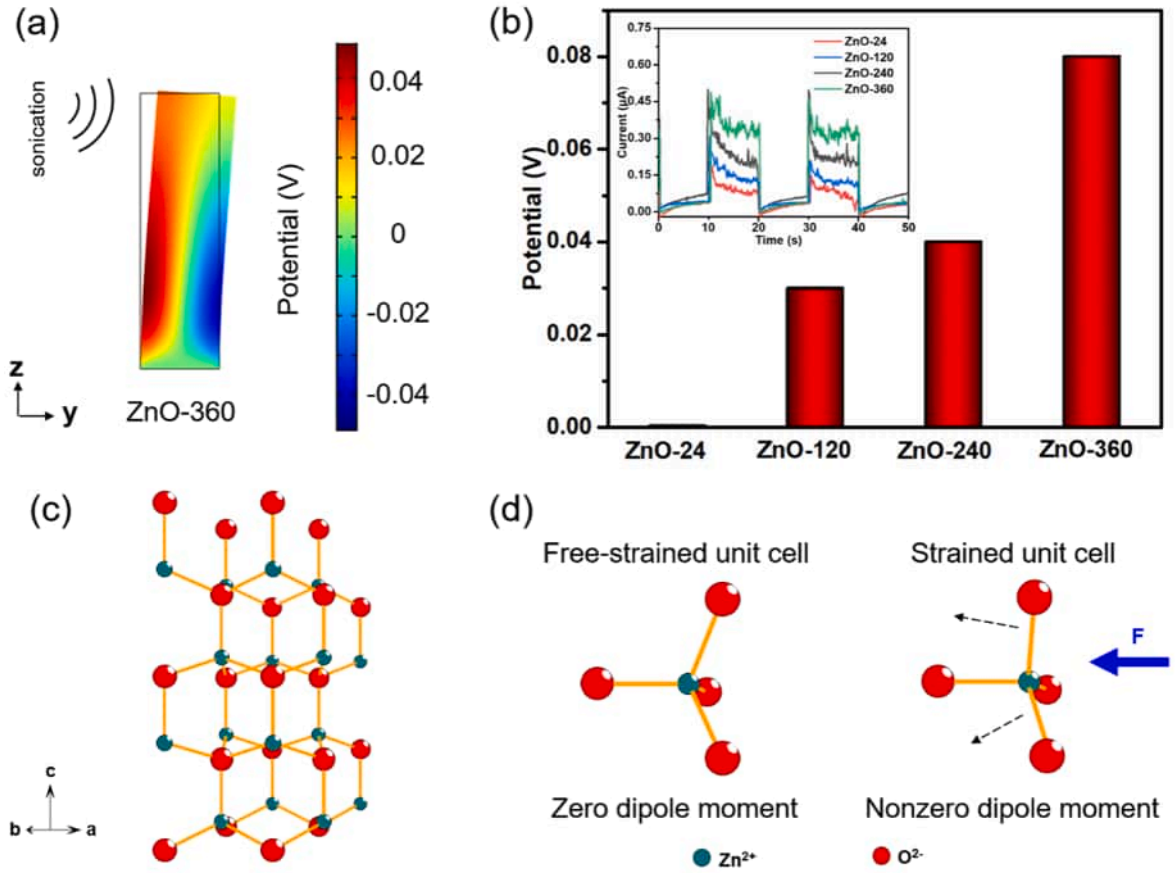

Fig. 3. (a) The piezoelectric potential distribution of ZnO-360; (b) piezo-potential of different samples; and the inset of b is the piezoelectric current response of different samples; (c) atomic structure of wurtzite ZnO crystal; (d) schematic illustration of piezoelectric effect in tetrahedrally coordinated cation–anion unit cell.

structure, which is the key to the generation of piezoelectric potential. As Fig. 3d shows, the Zn^{2+} cations and O^{2-} anions construct a tetrahedrally coordinated structure. When Zn–O dipoles are in a free-strain state, positive and negative charge centers overlap with each other, meaning that the dipole moment is zero. Yet, when the unit cell is endured by external stress, due to atomic displacement in domain switch, the Zn–O tetrahedra can deform, causing cation centers and anion centers are dislocated, generating a nonzero dipole moment [37]. Then, this structural summation of dipole moments created by all the unit cells in the crystal can form a macroscopic potential drop on the surface along the straining direction. Moreover, with the increasing proportion of polarization surfaces, greater piezoelectric potential can be accumulated and exported to manipulate the separation and migration of free carriers in an opposite direction, guiding separated carriers to participate in the catalytic reactions.

3.2. Study on the piezoelectric catalysis

To dig how the piezoelectric field affected the catalytic reactions, more detailed studies were performed and discussed as follows. The degradation kinetics of dyes were calculated based on the Langmuir-Hinshelwood model, and the degradation exhibited a pseudo-first-order kinetics reaction:

$$-\frac{d[Dye]}{dt} = k[Dye] \quad (1)$$

for $[Dye] = [Dye]_0$ at $t = 0$

$$\ln(\frac{[Dye]_0}{[Dye]}) = kt \quad (2)$$

where k is the pseudo-first-order rate constant.

3.2.1. Morphology-dependent piezoelectric-catalysis

In Fig. 4a-b, it is obvious that RhB cannot be degraded only with ultrasonic waves, implying that mechanical energy cannot be directly converted into chemical energy. Yet when the ZnO piezoelectric catalysts are added, ultrasonic waves, as a kind of mechanical energy, can make ZnO rods polarized and form a built-in piezoelectric field. Under the electric field, owning to strong electrostatic attraction, the PPD surface will draw compensating electrons toward the surface, while the NPD surface will repel electrons from the surface, as Eq. (3) shown [28].

$$ZnO + strain \rightarrow PPD(e^-) + NPD(h^+) \quad (3)$$

So, the carriers can be separated and migrate in an opposite direction for catalytic degradation (Fig. 4a-b). Interestingly, with the morphological sizes increasing from ZnO-24 to ZnO-360, the piezoelectric-catalytic activity and degradation rate (Fig. 4c) are enhanced, which is opposed to traditional cognition in the photocatalytic field that catalytic activity usually enhances with decreased sizes due to increased surface area [38,39]. The results should be related to the increasing proportion of polarization surfaces from ZnO-24 to ZnO-360 (Fig. 1). As Fig. 3b shows, if the exposure of polarization surfaces increases, a larger macroscopic potential drop can be formed along the straining direction, which is favorable to the separation and migration of piezo-generated carries for the catalytic reaction. In addition, larger polarization surfaces in polarized ZnO rods favor more pollutant molecules to be adsorbed in the activated domains, and then to be degraded efficiently. Therefore, the piezoelectric-catalytic activity enhances with the increasing exposure of polarization surfaces. In Fig. 4d, the ratios of aspect ratio/k rise firstly and then keep stable, indicating that the

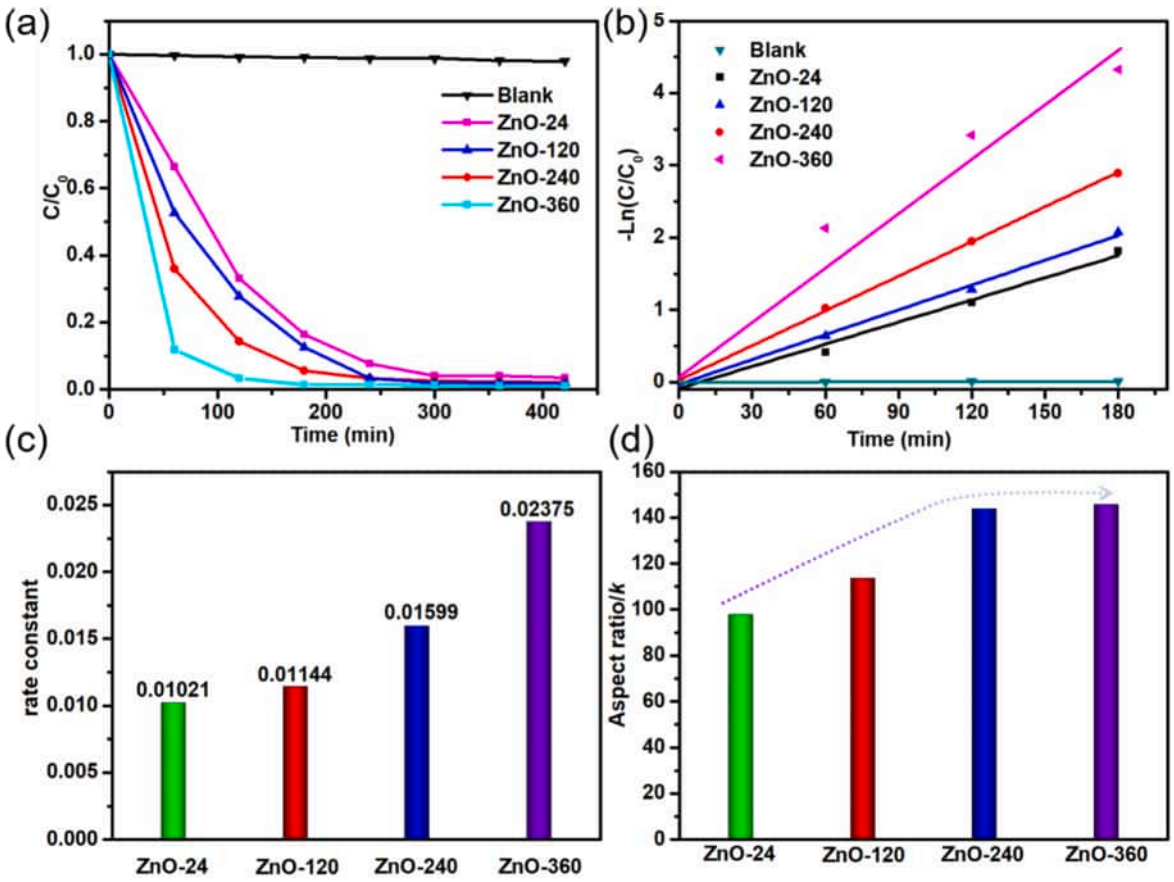

Fig. 4. (a) Piezoelectric-catalytic degradation curves of RhB and (b)(c) the first-order degradation rate constants with different samples; (d) the relationship between aspect ratio and rate constant *k*.

catalytic performance has weaker dependence on the polarization surfaces. With respect to ZnO-360, RhB can be degraded enormously within 60 min. Fig. S1 shows the typical change in the absorption spectra of RhB solutions during the piezoelectric-catalytic process.

3.2.2. Detection for active species of piezoelectric-catalysis and photocatalysis

Furthermore, different scavengers were used to detect the active species associated with selective adsorption and degradation of RhB (Fig. 5a-c). Besides, photocatalysis without strong electrostatic attraction was also carried out for comparison (Fig. 5d-f).

In Fig. 5a-c, the addition of CH_3OH greatly decreases the piezoelectric activity, indicating that h^+ is the most dominant species. This might result from that under the piezoelectric field, owing to electrostatic attraction, RhB, which is positively charged in water [40], can be selectively absorbed onto the NPD surface, where a great number of h^+ accumulate. Accordingly, RhB can be oxidized efficiently by h^+ due to selective adsorption [41]. In other words, in the piezoelectric catalytic process, the piezoelectric field in the polarized ZnO crystals can control the RhB molecules to be selectively absorbed onto the hole-gathering NPD surface because of the electrostatic attraction, achieving field-controlling selective adsorption, and this would facilitate the efficient reactions between RhB and h^+ (Eq. (4)), making holes as the most dominant species.

$$\mathrm{NPD}(h^+) + \mathrm{dye(RhB)} \rightarrow \mathrm{products} \quad (4)$$

On the contrary, RhB, as a kind of cationic dye, is always repelled by the PPD surface due to repulsive forces. Then the floating RhB dyes react with $^{\bullet}O_2^-$ or $^{\bullet}OH$ in the bulk solution in an inefficient way (See Eqs. (5)–(8)), making $^{\bullet}O_2^-$ and $^{\bullet}OH$ less important because of lacking good contact.

$$e^- + O_2 \rightarrow \hat{A}\cdot O_2^- \quad (5)$$

$$\hat{A}\cdot O_2^- + \mathrm{dye(floatingRhB)} \rightarrow \mathrm{products} \quad (6)$$

$$h^+ + H_2O \rightarrow \hat{A}\cdot OH \quad (7)$$

$$\hat{A}\cdot OH + \mathrm{dye(floatingRhB)} \rightarrow \mathrm{products} \quad (8)$$

In a word, under the piezoelectric field, it is due to the selective accumulation of h^+ and cationic RhB on the same NPD surface that holes become the most dominant species.

However, as for the photocatalysis without strong electrostatic attraction, the photooxidation with $^{\bullet}O_2^-$ floating in water dominates the catalytic reactions, making the photocatalytic efficiency lower than the piezoelectric catalytic efficiency (Fig. 5d-f). Lacking electrostatic attraction, the RhB molecules cannot be selectively adsorbed onto the NPD surface, so most RhB dyes float in the water and are degraded by floating $^{\bullet}O_2^-$ instead of h^+, which inefficient process may result in low activity and photo-corrosion from holes (discuss later). This result highlights the importance of selective adsorption for catalytic reactions.

3.2.3. Detection for active species using different cationic and anionic dyes

To further prove the field-controlling selective adsorption on corresponding charged surfaces, the cationic MB [16] and anionic MO [12] were also investigated in the ZnO system (Fig. 6). Also, $BaTiO_3$, as a typical piezoelectric material, was studied to confirm the generality of selective adsorption in the piezoelectric field (Fig. 7). In the cationic MB system, no matter the catalyst is ZnO or $BaTiO_3$, the addition of CH_3OH has the most influence on the piezoelectric activity, meaning that holes

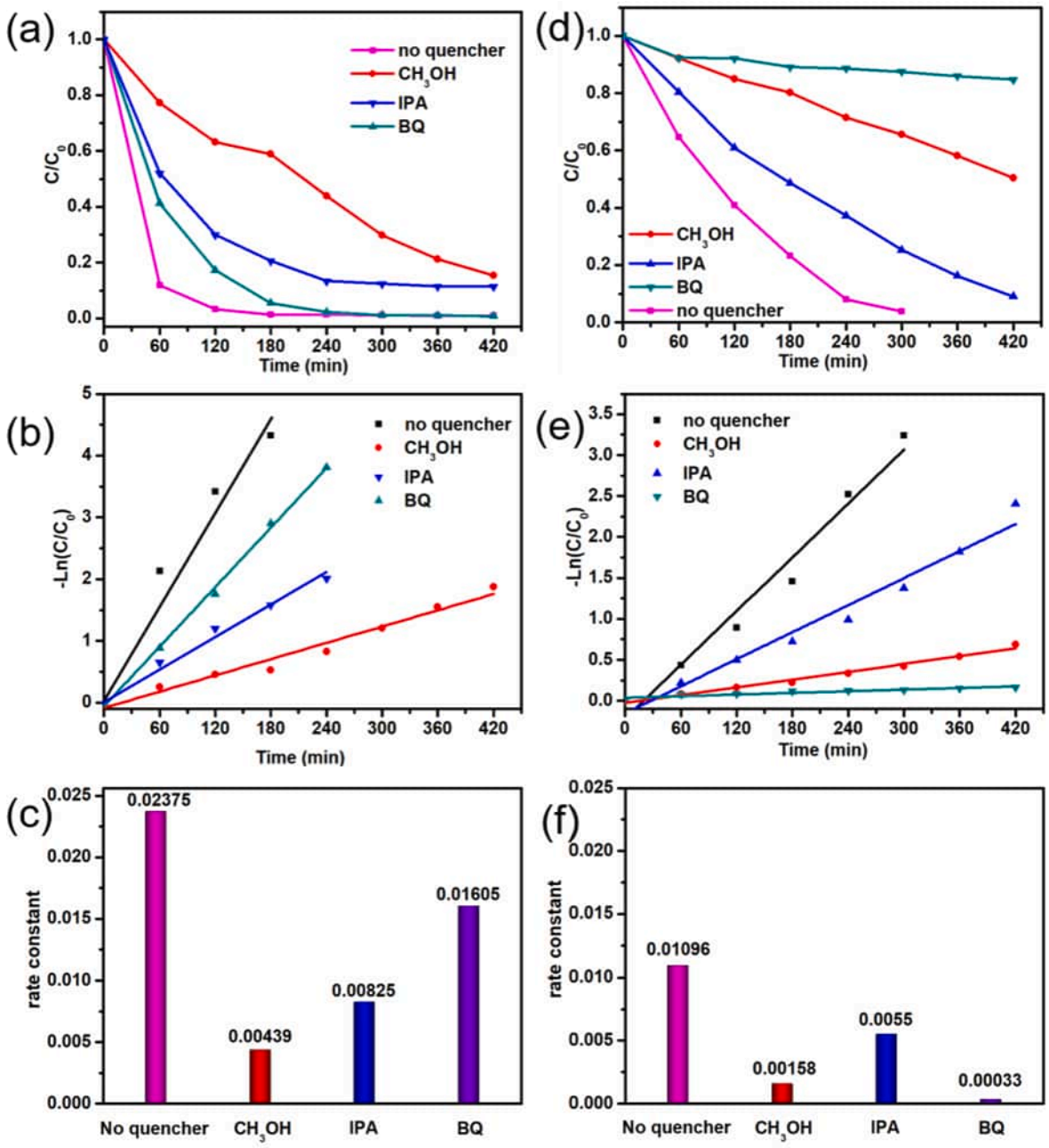

Fig. 5. (a) Piezoelectric-catalytic degradation curves of RhB and (b)(c) the first-order degradation rate constants with scavengers by using ZnO-360. (d) Photodegradation curves of RhB and (e)(f) the first order photodegradation rate constants with scavengers by using ZnO-360.

are the most dominant species in this kind of cationic-dye-system. Nevertheless, the addition of Na_2SO_4 or BQ has the least influence, implying that the effect of $^{\bullet}O_2^-$ species obtained by reducing the dissolved oxygen with e^- (Eq. (5)) can be ignorable. The above results declare that because of electrostatic attraction in the piezoelectric field, h^+ and cationic MB tend to selectively adsorb in the same NPD surface, realizing the efficient oxidation reaction. However, in the anionic MO system, the addition of Na_2SO_4 or BQ has the most influence. This is because that under the control of piezoelectric field, anionic MO dyes tend to selectively adsorb in electron-gathering PPD surface, where highly concentrated $^{\bullet}O_2^-$ species accumulate. Therefore, in the anionic-dye-system, piezo-generated electrons play the most important role.

All these results reveal a common principle that under the control of the piezoelectric field, the polarized surfaces tend to adsorb species with the opposite charge owing to the electrostatic attraction. Consequently, in the piezoelectric-catalytic process, cationic dyes tend to adsorb onto the hole-gathering NPD surface and can be oxidized by holes efficiently. Nevertheless, for the anionic dyes, they tend to adsorb onto the electron-gathering PPD surface for efficient reactions. These results mean that the piezoelectric field can optimize the molecular behavior according to the molecular polarity, achieving selective adsorption in the active catalytic zone to enhance catalytic performance.

3.2.4. *Compared the catalytic stability of piezoelectric-catalysis and photocatalysis*

Fig. 8 shows the recycling stability of ZnO-360 under the different excitation conditions. During the piezoelectric catalytic process, the piezoelectric catalytic performance is maintained over several cycles without any obvious changes. Nevertheless, the photocatalytic activity of ZnO-360 decreases obviously due to inherent hole attacks [42]. In the

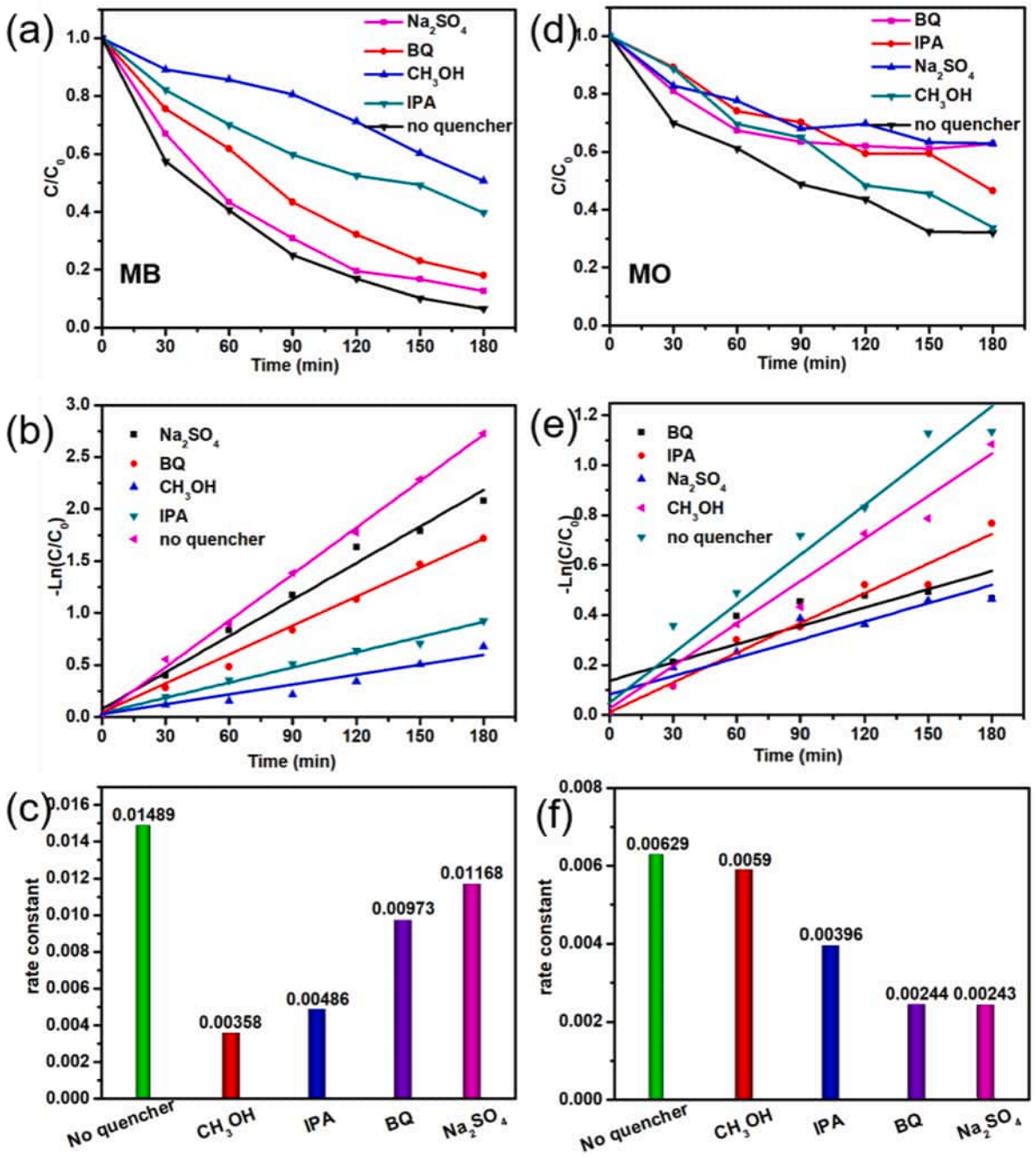

Fig. 6. (a) Piezoelectric-catalytic degradation curves and (b)(c) the related degradation rate constants with scavengers by using ZnO-360 in MB solution. (d) Photodegradation curves and (e)(f) the related photodegradation rate constants with scavengers by using ZnO-360 in MO solution.

photocatalytic process, photodegradation occurred mainly in the bulk solution via reacting with $^{\bullet}O_2^-$ instead of holes (Fig. 5). Thus, a great number of holes will be left to attack ZnO itself. Under the hole attacks, ZnO would suffer from the dissolution, which can be represented by Eq9 [41]:

$$ZnO + 2h^+ \rightarrow Zn^{2+} + 0.5O_2 \quad (9)$$

Based on Eqs. (4) and (9), it is known that the dissolution and catalytic degradation are two competitive pathways. For photocatalysis of ZnO-360, most of the photogenerated h^+ cannot participate in catalysis effectively due to poor adsorption (Fig. 5d-f), and then holes are left to attack ZnO itself, undergoing photo corrosion (Eq. (9)). However, for piezoelectric catalysis, thanks to electrostatic attraction, most of the piezo-generated h^+ can be consumed for the oxidation of RhB (Eq. (4)), which would suppress the corrosion from holes. Hence, due to piezo-induced selective electrostatic attraction, the catalytic degradation pathway can overcome the attack of holes, relieving the hole-sensitive symptom of ZnO, and making ZnO more robust and stable.

3.2.5. *Mechanism discussion*

The possible mechanism is described in Fig. 9. When the ZnO rod suffers external force, a nonzero dipole moment will be propagated, and the stretched side and the compressed side surfaces exhibit positive and negative piezo potential, respectively, forming a built-in electric field across the cross-section of a *c*-axis-oriented ZnO rod. Because the electric field is constructed by the non-mobile, non-annihilative ionic charges, thus these polarization charges (static and nonmobile) remain in the crystal as long as the stress remains [28,36]. In the piezoelectric field,

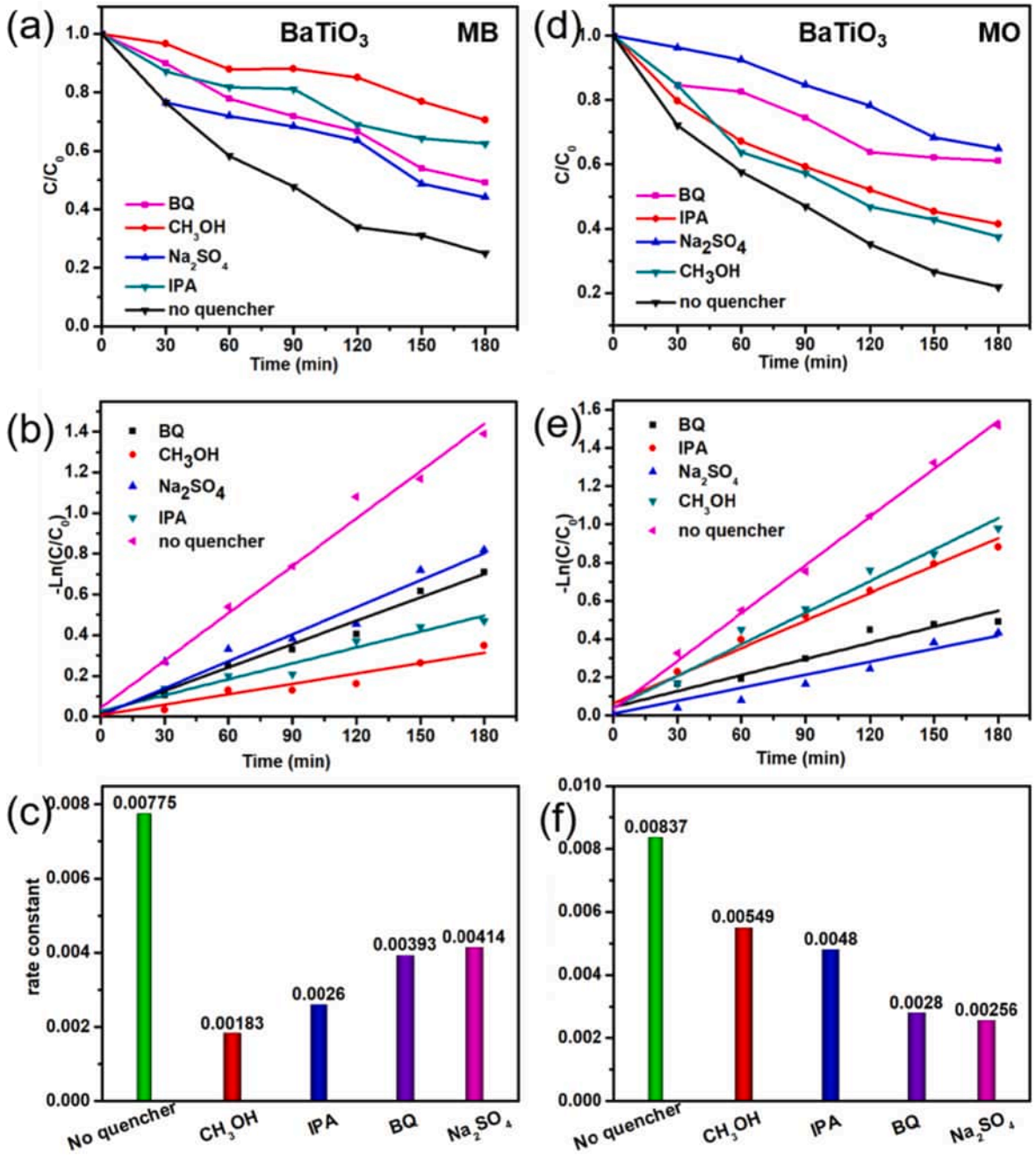

Fig. 7. (a) Piezoelectric-catalytic degradation curves and (b)(c) the related degradation rate constants with scavengers by using $BaTiO_3$ in MB solution. (d) Photodegradation curves and (e)(f) the related photodegradation rate constants with scavengers by using $BaTiO_3$ in MO solution.

PPD draws compensating electrons toward the surface, making the bandgap decrease here, while the NPD repels electrons from the surface, thus the bandgap increasing under a compressive strain [28]. Due to the piezo-induced inhomogeneous bandgap, charge carrier distribution and transfer can be manipulated for redox reactions. Furthermore, thanks to electrostatic attraction, the piezoelectric field can control the molecular behavior according to the molecular polarity. Specifically, cationic dyes tend to selectively accumulate onto the hole-gathering NPD surface, while anionic dyes tend to adsorb at the electron-gathering PPD surface, achieving the field-controlling selective adsorption, which makes holes and electrons play an important role in the cationic and anionic dyes systems, respectively, increasing the piezoelectric-catalytic performance due to the enhanced interaction between dye molecules and carriers. Therefore, polarized ZnO particle is just like a self-contained field controller and can manipulate the migration of carriers and dye molecules for enhanced piezoelectric-catalytic performance.

However, for other inefficient reaction paths, although these paths exist in the catalysis, they are not the most dominant reaction paths. Because it is selectivity-optimizing paths that dominate the piezoelectric catalysis, the piezoelectric-catalytic activity is far better than the activity of photocatalysis (Fig. 5), which unfortunately has to rely on the reactions with floating dyes owing to lacking strong electrostatic attraction.

3.2.6. *Piezo/photo-catalytic synergistic degradation*

Because ZnO is a specific dual responsive material, it can be excited by both strain and light. Thus, piezo/photo-catalytic degradation was carried out to monitor the synergistic effect. In Fig. 10a, under the light

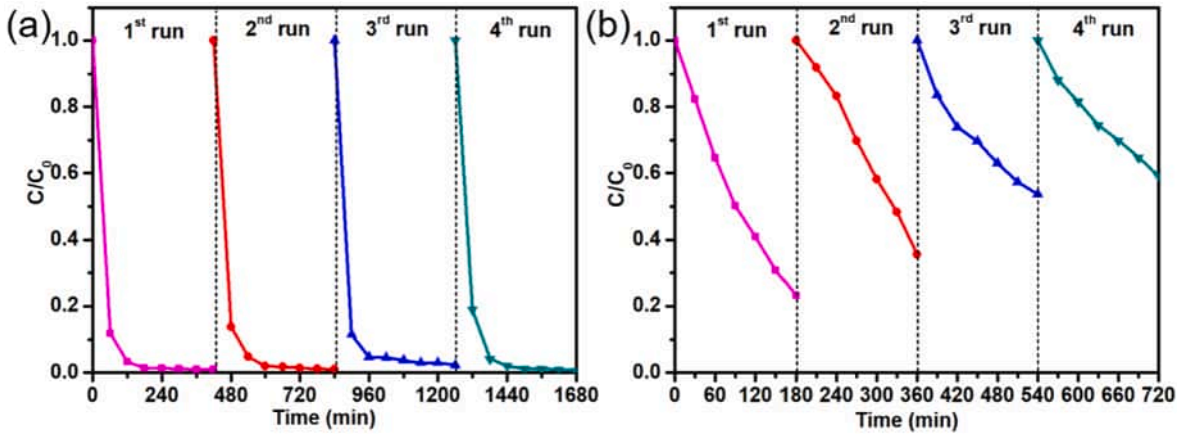

Fig. 8. The recycling stability of (a) piezoelectric catalytic and (b) photocatalytic reaction for RhB degradation using ZnO-360 microrods.

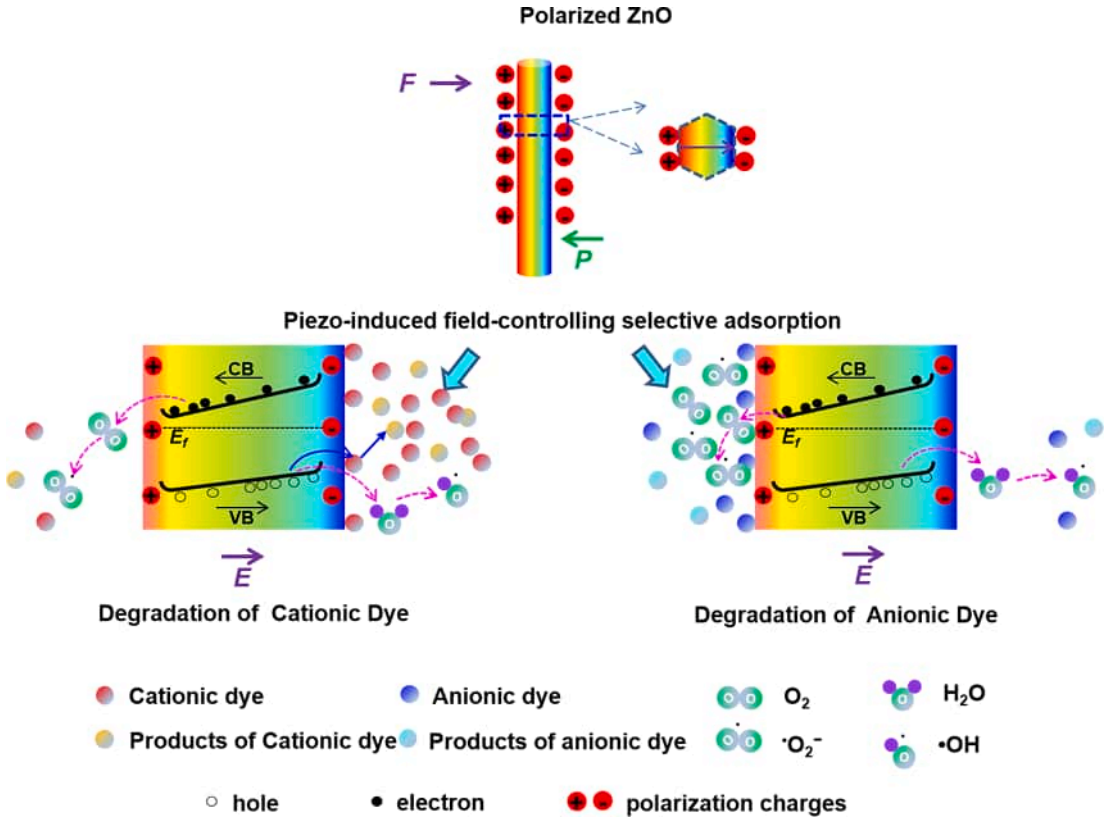

Fig. 9. Mechanism diagrams of selective adsorption and degradation for the piezoelectric catalysis.

irradiation, the photocatalytic activity decreases form ZnO-24 to ZnO-360, which should be associated with the decreasing surface areas (Fig. 1) and increasing probability of carrier recombination (Fig. S2). Nevertheless, when piezo and light synergistically stimulate the ZnO, the piezo-generated electric field can not only be used to drive the separation of free carriers but also guide the migration of dye molecules, optimizing the catalytic performance. Thus, the piezo/photo-catalytic activity of each sample is better than its photocatalytic activity. In addition, with an increasing proportion of polarization surfaces from ZnO-120 to ZnO-360, the enhancing macroscopic potential drop can be employed to separate the carriers, improving the catalytic activity (Fig. 10b). For ZnO-24, its better piezo/photo-catalytic activity should be attributed to its much larger surface area (Fig. 1). Besides, it can be found that ZnO can work stably after several cycles (Fig. 10c), which might result from that holes have been immensely consumed for catalysis due to field-controlling selective adsorption, overcoming the photo corrosion pathway, as shown in Fig. 10d. Thus, ZnO, as a dual responsive catalyst, can be more efficient and robust under the dual stimulation from light and mechanical waves.

4. Conclusion

In conclusion, ZnO rods with the different proportions of polarization surfaces were tailored to optimize piezoelectric catalytic performance, and an interesting phenomenon of field-controlling selective adsorption has been discovered for the first time. Due to the field-controlling selective adsorption, the piezoelectric-catalytic activity of ZnO-360 is better than its photocatalytic activity. Besides, this selective

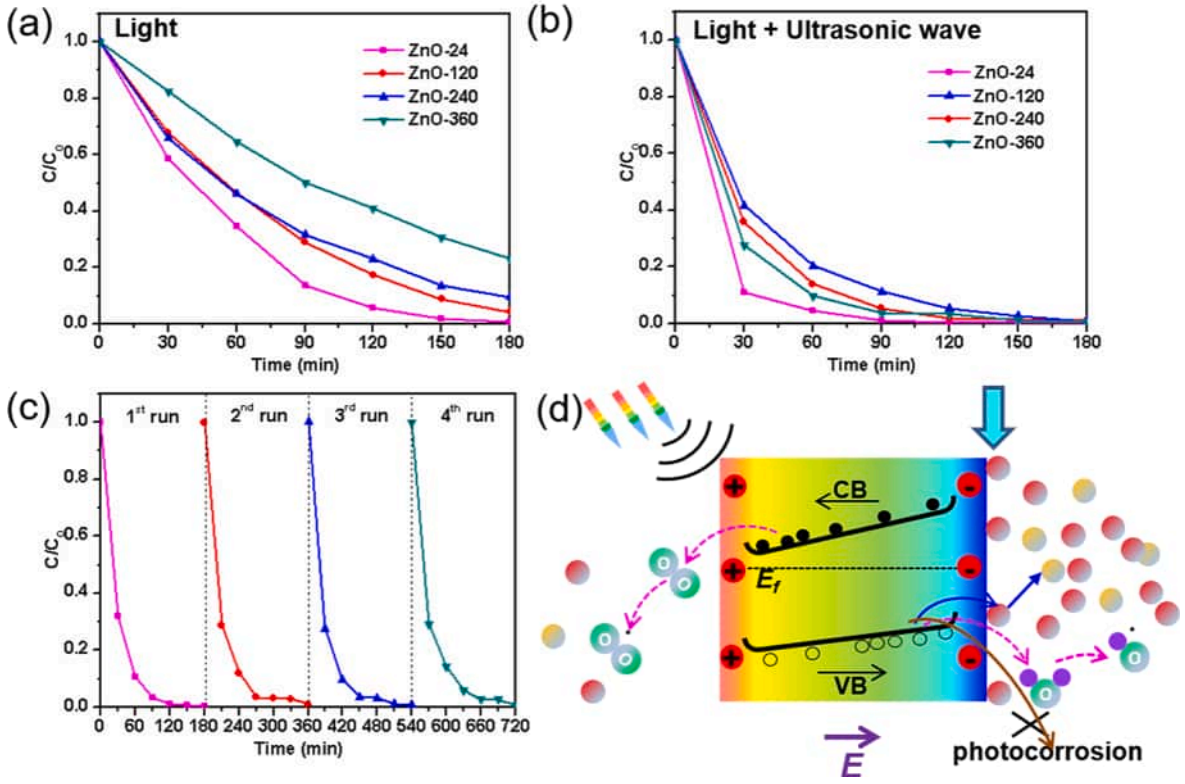

Fig. 10. (a) Photo-catalytic degradation curves of RhB; (b) piezo/photo-catalytic degradation curves of different ZnO samples in RhB solution; (c) the recycling stability of piezo/photo-catalytic reaction using ZnO-360 microrods in RhB solution; (d) piezo/photo-catalytic synergistic mechanism.

adsorption can also be used to relieve the hole-sensitive symptoms of ZnO and improve its stability of RhB degradation. Furthermore, ZnO rods, as a dual responsive catalyst, can be more efficient and robust under the synergistic excitation from light and mechanical waves. Moreover, our present work will broaden the horizon and provide a new general strategy to design various field-controlling selective adsorption systems for wide applications, such as biological diagnosis, drug delivery, and so on.

CRediT authorship contribution statement

Fengping Peng: Conceptualization, Investigation, Data curation, Formal analysis, Writing - original draft. **Haozhen Li:** Investigation, Formal analysis. **Wanxin Xu:** Investigation, Formal analysis. **Huihua Min:** Investigation, Resources. **Zhenxuan Li:** Resources. **Feihu Li:** Resources, Resources. **Xiaogu Huang:** Conceptualization, Resources, Funding acquisition. **Wei Wang:** Conceptualization, Resources, Writing - review & editing. **Chunhua Lu:** Resources, Supervision.

Declaration of Competing Interest

The authors declare that they have no known competing financial interests or personal relationships that could have appeared to influence the work reported in this paper.

Acknowledgements

Financial support from National Natural Science Foundation of China (No. 51809140, 51502143, 41303096, 51608277), Natural Science Foundation of Jiangsu Province (No. BK20180793, BK20170954), Jiangsu Government Scholarship for Overseas Studies, Innovation and Entrepreneurship Training Program for College Students of Jiangsu Province, Jiangsu Students' Platform for innovation and entrepreneurship training program (No. 201910300088Y), NUIST Students' Platform for Innovation and Entrepreneurship Training Program, College Students' Enterprise and Entrepreneurship Education Program of NUIST (CSEEEP), the Natural Science Foundation of Jiangsu Higher Education Institutions of China (No. 17KJB430023), the Startup Foundation for Introducing Talent of NUIST (No. 2243141701032, 2017r032), Postgraduate research and Practical Innovation Plan of Jiangsu Province (KYCX18_1030), the Priority Academic Program Development of the Jiangsu Higher Education Institutions (PAPD) is gratefully acknowledged.

Appendix A. Supplementary data

Supplementary data to this article can be found online at https://doi.org/10.1016/j.apsusc.2021.149032.

References

[1] M. Zhou, Z. Wang, Q. Sun, J. Wang, C. Zhang, D. Chen, X. Li, High-performance Ag-Cu nanoalloy catalyst for the selective catalytic oxidation of ammonia, ACS Appl. Mater. Interfaces 11 (2019) 46875–46885.
[2] Z. Wang, Q. Sun, D. Wang, Z. Hong, Z. Qu, X. Li, Hollow ZSM-5 zeolite encapsulated Ag nanoparticles for SO_2-resistant selective catalytic oxidation of ammonia to nitrogen, Sep. Purif. Technol. 209 (2019) 1016–1026.
[3] Y. Lin, J. Sun, S. Li, D. Wang, C. Zhang, Z. Wang, X. Li, An efficient Pt/Ce$yCoO_x$ composite metal oxide for catalytic oxidation of toluene, Catal. Lett. 150 (2020) 3206–3213.
[4] S. Li, Y. Lin, D. Wang, C. Zhang, Z. Wang, X. Li, Polyhedral cobalt oxide supported Pt nanoparticles with enhanced performance for toluene catalytic oxidation, Chemosphere 263 (2021) 127870.
[5] J. Liu, J. Li, Y. Li, J. Guo, S.M. Xu, R. Zhang, M. Shao, Photoelectrochemical water splitting coupled with degradation of organic pollutants enhanced by surface and interface engineering of $BiVO_4$ photoanode, Appl. Catal. B 278 (2020) 119268.
[6] Y. Kim, M. Watanabe, J. Matsuda, J.T. Song, A. Takagaki, A. Staykov, T. Ishihara, Tensile strain for band engineering of $SrTiO_3$ for increasing photocatalytic activity to water splitting, Appl. Catal. B 278 (2020) 119292.
[7] J. Qin, Z. Liu, D. Wu, J. Yang, Optimizing the electronic structure of cobalt via synergized oxygen vacancy and Co-N-C to boost reversible oxygen electrocatalysis for rechargeable Zn-air batteries, Appl. Catal. B 278 (2020) 119300.

[8] S. Cestellos-Blanco, H. Zhang, J.M. Kim, Y. x. Shen, P. Yang, Photosynthetic semiconductor biohybrids for solar-driven biocatalysis, Nat. Catal., 3 (2020) 245-255.
[9] H.X. Kuang-Sheng Hong, Hiromi Konishi, Xiaochun Li, Direct water splitting through vibrating piezoelectric microfibers in water, J. Phys. Chem. Lett 1 (2010) 997–1002.
[10] J.M. Wu, W.E. Chang, Y.T. Chang, C.K. Chang, Piezo-catalytic effect on the enhancement of the ultra-high degradation activity in the dark by single- and few-Layers MoS_2 nanoflowers, Adv. Mater. 28 (2016) 3718–3725.
[11] Y. Wang, X. Wen, Y. Jia, M. Huang, F. Wang, X. Zhang, Y. Bai, G. Yuan, Y. Wang, Piezo-catalysis for nondestructive tooth whitening, Nat. Commun. 11 (2020) 1328.
[12] Z. Kang, N. Qin, E. Lin, J. Wu, B. Yuan, D. Bao, Effect of Bi_2WO_6 nanosheets on the ultrasonic degradation of organic dyes: roles of adsorption and piezocatalysis, J. Cleaner Prod. 261 (2020) 121125.
[13] A. Kakekhani, S. Ismail Beigi, Polarization-driven catalysis via ferroelectric oxide surfaces, PCCP 18 (2016) 19676–19695.
[14] S. Dag, S. Wang, L.W. Wang, Large surface dipole moments in ZnO nanorods, Nano Lett. 11 (2011) 2348–2352.
[15] Z. LinWang, Piezotronic and piezophototronic effects, J. Phys. Chem. Lett. 1 (2010) 1388–1393.
[16] A. Gurses, C. Dogar, M. Yalcin, M. Acikyildiz, R. Bayrak, S. Karaca, The adsorption kinetics of the cationic dye, methylene blue, onto clay, J. Hazard. Mater. 131 (2006) 217–228.
[17] J. Hu, Y. Fan, Y. Pei, M. Qiao, K. Fan, X. Zhang, B. Zong, Shape effect of ZnO crystals as cocatalyst in combined reforming–hydrogenolysis of glycerol, ACS Catal. 3 (2013) 2280–2287.
[18] Z. Chen, Q. Zhang, Y. Luo, Experimental identification of ultrafast reverse hole transfer at the interface of the photoexcited methanol/graphitic carbon nitride system, Angew. Chem. 57 (2018) 5320–5324.
[19] S. Tu, H. Huang, T. Zhang, Y. Zhang, Controllable synthesis of multi-responsive ferroelectric layered perovskite-like $Bi_4Ti_3O_{12}$: Photocatalysis and piezoelectric-catalysis and mechanism insight, Appl. Catal. B 219 (2017) 550–562.
[20] H. Zouch, F. Karray, F. Armougom, S. Chifflet, A. Hirschler-Rea, H. Kharrat, L. Kamoun, W. Ben Hania, B. Ollivier, S. Sayadi, M. Quemeneur, Microbial diversity in sulfate-reducing marine sediment enrichment cultures associated with anaerobic biotransformation of coastal stockpiled phosphogypsum (Sfax, Tunisia), Front. Microbiol. 8 (2017) 1583.
[21] A.H. Kaksonen, J.J. Plumb, P.D. Franzmann, J.A. Puhakka, Simple organic electron donors support diverse sulfate-reducing communities in fluidized-bed reactors treating acidic metal- and sulfate-containing wastewater, FEMS Microbiol. Ecol. 47 (2004) 279–289.
[22] F.C. Kim, A. Deweerd, Joseph M. Suflita, Relationship between hydrogen consumption, dehalogenation, and the reduction of sulfur oxyanions by desulfomonile tiedjei, Appl. Environm. Microbiol., 57 (1991) 1929-1934.
[23] O.V. Karnachuk, S.Y. Kurochkina, O.H. Tuovinen, Growth of sulfate-reducing bacteria with solid-phase electron acceptors, Appl. Microbiol. Biotechnol. 58 (2002) 482–486.
[24] R.U. Meckenstock, Fermentative toluene degradation in anaerobic defined syntrophic cocultures, FEMS Microbiol. Lett. 177 (1999) 67–73.
[25] T.J. Athauda, R.R. Ozer, Nylon fibers as template for the controlled growth of highly oriented single crystalline ZnO nanowires, Cryst. Growth Des. 13 (2013) 2680–2686.
[26] A.R. Azulay, Y. Turkulets, D.D. Gaudio, R.S. Goldman, I. Shalish, Why do nanowires grow with their c-axis vertically-aligned in the absence of epitaxy? Sci. Rep. 10 (2020).
[27] X. Xue, W. Zang, P. Deng, Q. Wang, L. Xing, Y. Zhang, Z.L. Wang, Piezo-potential enhanced photocatalytic degradation of organic dye using ZnO nanowires, Nano Energy 13 (2015) 414–422.
[28] S. Xu, W. Guo, S. Du, M.M. Loy, N. Wang, Piezotronic effects on the optical properties of ZnO nanowires, Nano Lett. 12 (2012) 5802–5807.
[29] D.E. Motaung, G.H. Mhlongo, S.S. Nkosi, G.F. Malgas, B.W. Mwakikunga, E. Coetsee, H.C. Swart, H.M. Abdallah, T. Moyo, S.S. Ray, Shape-selective dependence of room temperature ferromagnetism induced by hierarchical ZnO nanostructures, ACS Appl. Mater. Interfaces, (2014).
[30] E.S. Jang, J.H. Won, S.J. Hwang, J.H. Choy, Fine tuning of the face orientation of ZnO crystals to optimize their photocatalytic activity, Adv. Mater. 18 (2006) 3309–3312.
[31] B. Cheng, E.T. Samulski, Hydrothermal synthesis of one-dimensional ZnO nanostructures with different aspect ratios, Chem. Commun. (2004) 986–987.
[32] A.-W.X. Yin Peng, Bin Deng, Markus Antonietti, Helmut Colfen, Polymer-controlled crystallization of zinc oxide hexagonal nanorings and disks, J. Phys. Chem. B 110 (2006) 2988–2993.
[33] T.H.G.R. Li, G.L. Pan, T.Y. Yan, X.P. Gao, H.Y. Zhu, Morphology-function relationship of ZnO: polar Planes, oxygen Vacancies, and activity, J. Phys. Chem. C 112 (2008) 11859–11864.
[34] K. Sun, Y. Jing, C. Li, X. Zhang, R. Aguinaldo, A. Kargar, K. Madsen, K. Banu, Y. Zhou, Y. Bando, Z. Liu, D. Wang, 3D branched nanowire heterojunction photoelectrodes for high-efficiency solar water splitting and H_2 generation, Nanoscale 4 (2012) 1515–1521.
[35] B. Jiang, J. Iocozzia, L. Zhao, H. Zhang, Y.W. Harn, Y. Chen, Z. Lin, Barium titanate at the nanoscale: controlled synthesis and dielectric and ferroelectric properties, Chem. Soc. Rev. 48 (2019) 1194–1228.
[36] Z.L. Wang, J. Song, Piezoelectric nanogenerators based on zinc oxide nanowire arrays, Science 312 (2006) 242–246.
[37] Z.L. Wang, Piezopotential gated nanowire devices: piezotronics and piezo-phototronics, Nano Today 5 (2010) 540–552.
[38] S. Wang, M. Xu, T. Peng, C. Zhang, T. Li, I. Hussain, J. Wang, B. Tan, Porous hypercrosslinked polymer-TiO_2-graphene composite photocatalysts for visible-light-driven CO_2 conversion, Nat. Commun. 10 (2019) 676.
[39] A. Islam, S. Hwa Teo, M.R. Awual, Y.H. Taufiq-Yap, Ultrathin assembles of porous array for enhanced H_2 evolution, Sci. Rep. 10 (2020) 2324.
[40] J. Kim, Y. Park, H. Park, Solar hydrogen production coupled with the degradation of a dye pollutant using TiO_2 modified with platinum and nafion, Int. J. Photoenergy 2014 (2014) 1–9.
[41] H.C. Liwu Zhang, Ruilong Zong, Yongfa Zhu, Photocorrosion suppression of ZnO nanoparticles via hybridization with graphite-like carbon and enhanced photocatalytic activity, J. Phys. Chem. C 113 (2009) 2368–2374.
[42] R.Z. Hao Zhang, Yongfa Zhu, Photocorrosion inhibition and photoactivity enhancement for Zinc Oxide via hybridization with monolayer polyaniline, J. Phys. Chem. C 113 (2009) 4605–4611.